Research paper

Dating the setting of a late prehistoric statue-menhir at Cruz de Cepos, NE Portugal

I.K. Bailiff [a,*], E. Andrieux [a], M. Díaz-Guardamino [a], L.B. Alves [b], B. Comendador Rey [c], L. García Sanjuán [d], Maria Martín Seijo [e]

[a] Department of Archaeology, Durham University, South Road, Durham, DH1 3LE, UK
[b] Centre of Studies on Archaeology, Arts and Heritage Sciences (CEAACP)/FCT, University of Coimbra, Portugal
[c] Grupo de Estudios de Arqueología, Antigüedad y Territorio (GEAAT), University of Vigo, Spain
[d] Department of Archaeology and Prehistory, University of Sevilla, Spain
[e] Instituto de Ciencias del Patrimonio, Consejo Superior de Investigaciones Científicas – INCIPIT-CSIC, Edificio Fontán, Santiago de Compostela, Spain

A B S T R A C T

The emergence of 'standing stone' monuments within the European Late Prehistoric landscape is considered to be associated with a pivotal human cultural transition from hunting and gathering to agriculture and permanent settlement, being the earliest monuments currently dated by radiocarbon to the 5th millennium BCE. However, many standing stones were first erected, subsequently collapsed, and then re-erected during the following three millennia. The excavation of the site of an apparently in situ statue-menhir at Cruz de Cepos in NE Portugal provided the rare opportunity in Iberian prehistory to apply radiocarbon and luminescence techniques to establish the date of construction. On the basis of the iconography, the standing stone was assigned to a sculptural tradition of north-western and western Iberia, loosely dated to the Early/Middle Bronze Age (ca. 2000/1900–1250 BCE). The optically stimulated luminescence (OSL) and dosimetry characteristics of quartz extracted from sediment samples taken from locations associated with the socket pit and surrounding backfilling deposits were examined, producing OSL single grain ages at eight locations. Comparison of the OSL and calibrated radiocarbon ages shows very good agreement, with the mid-3rd millennium BCE dates confirming original erection during the Copper Age and not a much later transformation of the monument. These encouraging results indicate that OSL has the potential to provide reliable dating of depositional processes related to the construction process and is suitable for wider application to megalithic monuments of this type.

1. Introduction

Standing stones form an important component of prehistoric stone monumentality that is commonly found in Eurasia. Although they occur on sites as early as 9600 BCE, notably at the site of Göbekli Tepe in SE Turkey, the earliest evidence in western Europe is much later, found in NW France such as the Breton sites on the island of Hoedic and at Locmariaquer in Carnac, which are dated to c. 4700-4500 BCE (Cassen, 2009; Large and Mens, 2016). The archaeological significance of the earliest standing stones lies in their appearance in connection with the transition to farming in western Eurasia (Calado, 2002; Large and Mens, 2016; Whittle, 2002). Although there are thousands of such monuments in western Iberia, dating their erection has been problematic because of issues related to contextual evidence and complexities in taphonomic processes obscuring whether organic samples potentially suitable for radiocarbon dating can be securely associated with the construction process. An opportunity to examine the potential of optically stimulated luminescence (OSL) to date the setting of a monolith arose with the excavation of the base of a late prehistoric statue-menhir (i.e., a standing stone with three-dimensional human form) found at the site of Cruz de Cepos, in NE Portugal. From its engraved iconography, the statue-menhir appeared to date to the Bronze Age, as it includes the depiction in low relief of a sword (Alves and Reis, 2011: 197, Figs. 4–5) (Fig. 1). Long daggers, such as those found in northwest Iberia in the funerary cists of Atios (L: 31 cm) (Pontevedra), Carnota (L: 28 cm) or Santa Comba (L: 36 cm) (A Coruña), are dated between the late 3rd and the early 2nd millennium BC (Brandherm, 2003; Comendador Rey, 1995: 123–128). The earliest swords in Iberia (made of copper with
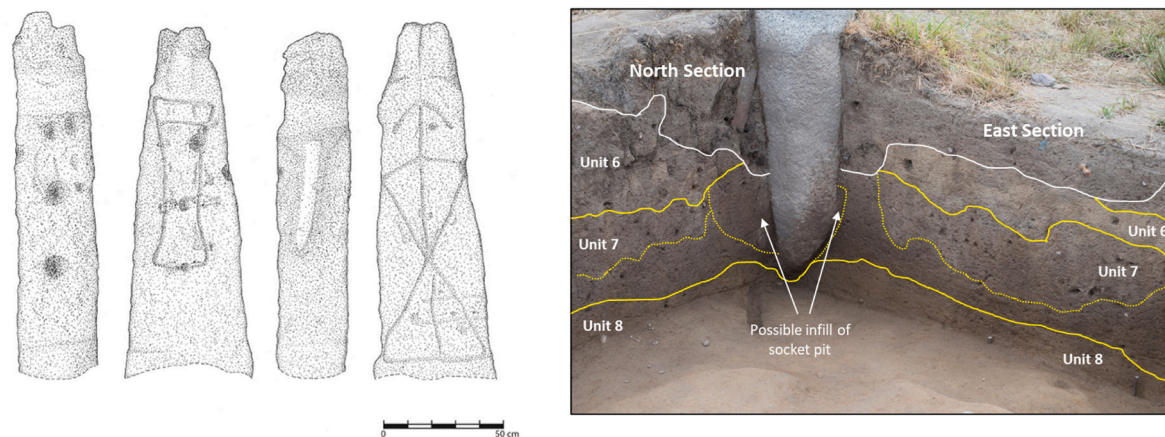
Fig. 1. Left: The statue-menhir of Cruz de Cepos as recorded in the early 2000s (Length of the sword: 50 cm) (Alves and Reis 2011: Fig. 5). Right: Image of the excavation trench showing the lower part of the statue-menhir set in its socket, overlain with the interpreted boundaries of depositional units, as shown in more detail in the North and East sections (Fig. 2).

arsenic content), such as Pinhal dos Melos (Beira Alta, north Portugal, L: 57 cm; Jorge, 1995: 31) or Villaviudas I (Palencia, north Spain, L: 51 cm; Gómez Ramos, 2001), situated within the Early Bronze Age, from ca. 2000/1900 BCE, can be used as a *termini post quem* for their representation on stone monuments such as the statue-menhir of Cruz de Cepos (Alves and Reis, 2011: 197). However, a key question is dating when the standing stone was first erected in its current location to establish whether it formed part of a broader pattern of reuse or re-siting of Neolithic and Copper Age monuments (Bueno Ramirez et al., 2016, 2019). In this paper we discuss a pilot study that examines the potential of OSL to establish a chronology for the setting of this type of monument and to compare the OSL age estimates with the results of radiocarbon testing of organic material recovered from associated sealed contexts.

2. The site

The Cruz de Cepos statue-menhir is located in the field of Padrão (41.74986° North; −7.67442° West), standing in the middle of a high plateau, serving as a boundary marker between the municipalities of Arcos and Cervos, in NE Portugal. First recorded as an element "with patterns" in the early 20th century, it was later recognized as a prehistoric three-dimensional sculpture of a human figure (Díaz-Guardamino, 2010: 163−169; Alves and Reis, 2011) and assigned to a sculptural tradition of north-western and western Iberia, loosely dated to the

Early/Middle Bronze Age (ca. 2000/1900–1250 BCE) (Alves and Reis, 2011: 206; see also Díaz-Guardamino, 2010: Ch 7.1; Díaz-Guardamino et al., n.d.). The rounded and worked smooth surface of the buried base of the statue-menhir revealed by excavation is redolent of Neolithic standing stones of the region (Gomes, 1993). The stone is a coarse two-mica granite which is commonly found in the area in many accessible outcrops, some with clear signs of quarrying, although of indeterminate age of working. A more specific provenance of the monolith requires further investigation by petrographic analysis.

3. Excavation and sampling

The site was first investigated in 2009 by Alves and Reis (2011) through surface survey and targeted excavation. A test pit (1.20 × 0.50 m) was excavated at the north side of the visible base of the statue-menhir, reaching the base of the monolith at around 1m depth, and after detecting a stratigraphic unit (UE5) congruent with a possible setting pit with archaeological materials of prehistoric date. From 2016 to 2019, a team lead by L.B. Alves, M. Díaz-Guardamino, and B. Comendador conducted four seasons of fieldwork consisting of survey (geophysics, fieldwalking) and excavation of four trenches (Diaz-Guardamino et al., in prep). A trench (Trench 1) was set at the south-west base of the statue-menhir, measuring 3.70 × 2 m, to further investigate the monument and its surrounding deposits (Fig. 1). The
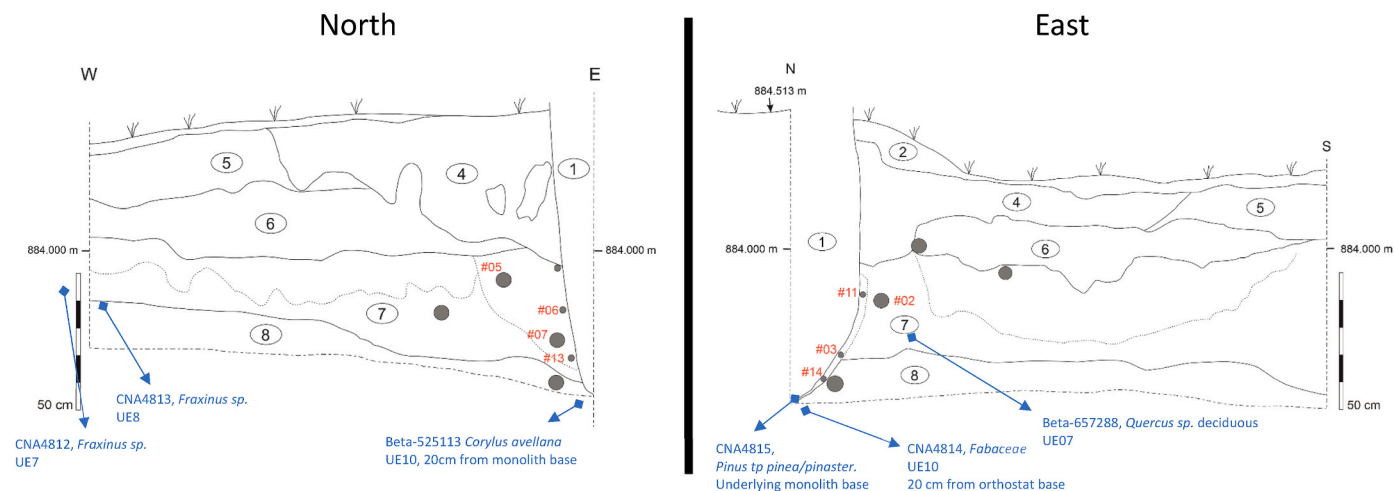

Fig. 2. North and east sections of the excavated trench showing the assigned stratigraphic units (encircled numbers), the lower part of the standing stone (①) and the locations of OSL (filled circles) and radiocarbon (filled diamonds) samples.
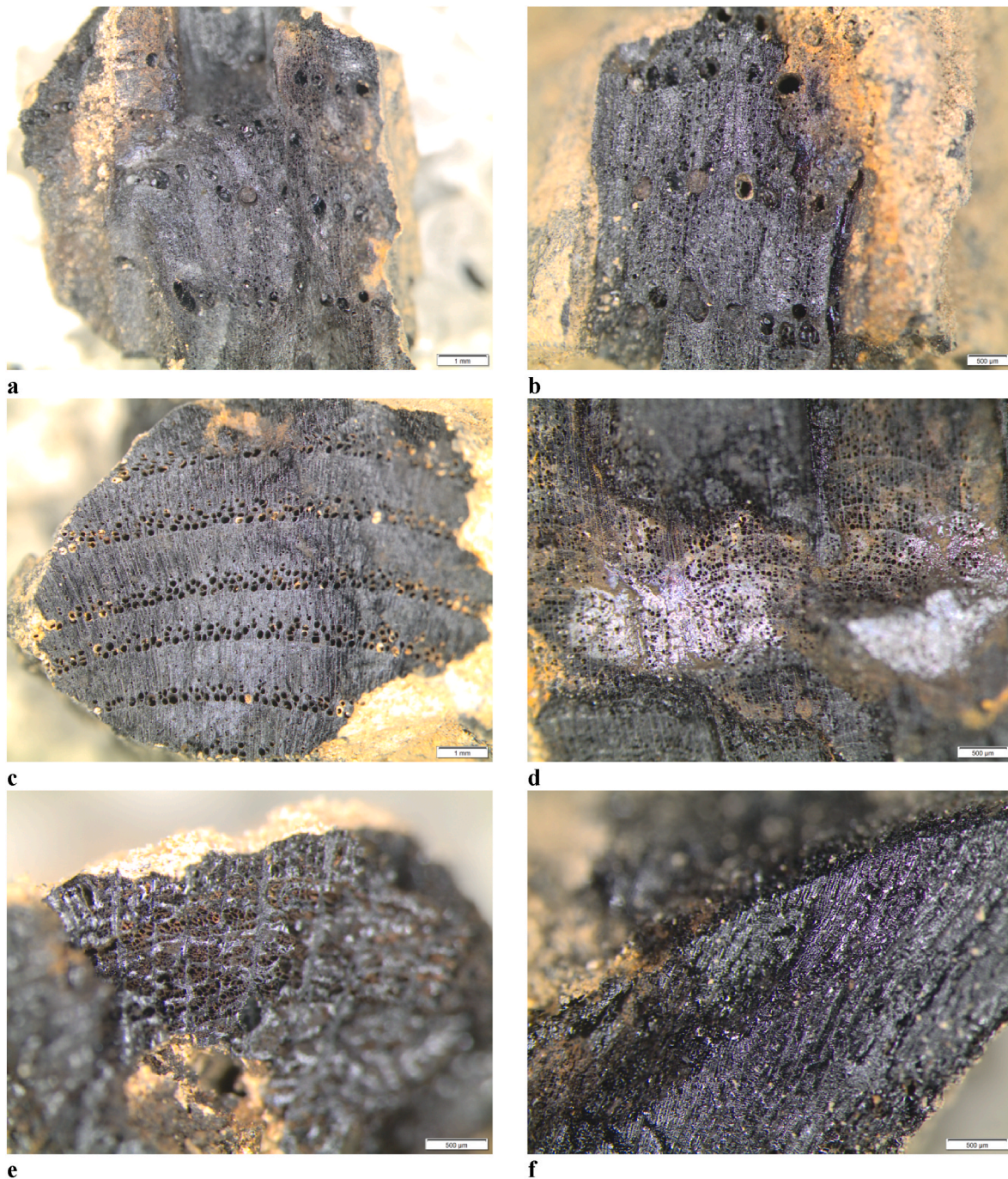
Fig. 3. Cross sections of charcoal samples submitted for radioacarbon dating. a-b) *Quercus* sp. deciduous, c) *Fraxinus* sp., d) *Corylus avellana*, e) Fabaceae and f) *Pinus* tp. *pinea/pinaster*.

excavation revealed a sequence of depositional phases, including the basal section of a socket pit into which the stone had been inserted. Assessment of the soil structure of unit 7 (UE7) elsewhere within the trench indicated mixing by (ancient) ploughing activity in its upper part (Fig. 1, marked with discontinuous line). Units 7 and 8 (UE7, UE8) both yielded prehistoric material, including fragments of hand thrown pottery, charcoal, quartzite and quartz flakes and a rock crystal prism. OSL samples were extracted using 40 mm and 20 mm diameter opaque plastic tubes from deposits adjacent to two faces of the lower part of the monolith and into the North and East sections, as indicated in Fig. 2. The eight numbered locations correspond to the OSL samples analysed and for which age estimates were obtained. Five of the smaller tubes located in close proximity to the standing stone base were inserted taking care to

avoid abrasion of the lithic surface.

Of the 19 archaeobotanical samples analysed, all contained charcoal. Ninety-one fragments were taxonomically identified following the standard procedure (Cartwright 2015), and dendrological and taphonomic attributes (Marguerie and Hunot 2007) were registered in tandem. From this assemblage, five charred wood samples primarily of short-lived specimens were selected for radiocarbon dating (Table 3). They included sorted twigs from shrubs such as those of the Fabaceae family (CAN4814) and hazel (*Corylus avellana*; Beta 525113). Of the fragments derived from trees, the samples with moderate to strong annual tree-ring curvature, and likely to be from twigs or young branches, were selected (Fig. 3 c-f). This was the case for the samples of ash (*Fraxinus* sp.; CNA4812 and CAN4813) and stone/maritime pine

Table 1
Data used in the calculation of the OSL depositional age.

Sample Dur_	Section	n	OD	Skewness	Model	$\overline{D}_e$	$\dot{D}_\beta$	$\dot{D}_\gamma$	$\dot{D}_c$	$\dot{D}_{tot}$	OSL Age	$\pm\sigma_A$	$\pm\sigma_{OE}$
			(%)	c (%c_{crit})		(Gy)	(mGy a^{-1})				(a)	(a)	(a)
446–2	E	132/223	19 ± 2	0.32(76)	CDM	17.93 ± 0.33	2.18	1.31	0.20	3.69 ± 0.15	4860	215	360
			17 ± 1	−0.10(24)	"	17.81 ± 0.31							
446–3	E	127/200	30 ± 2	0.83(190)	MDM	17.11 ± 1.14	2.35	1.27	0.20	3.83 ± 0.15	4470	345	435
446–5	N	184/273	14 ± 1	−0.14(39)	CDM	16.27 ± 0.20	2.05	1.28	0.20	3.53 ± 0.14	4610	195	335
446–6	N	216/296	15 ± 1	0.62(187)	CDM	15.89 ± 0.19	2.05	1.20	0.20	3.45 ± 0.14	4605	190	335
		215	13 ± 1	0.09(27)	CDM	15.82 ± 0.17							
446–7	N	139/227	12 ± 1	−0.07(17)	CDM	15.74 ± 0.21	2.05	1.23	0.20	3.49 ± 0.14	4510	190	330
446–11	E	184/254	18 ± 1	−0.17(47)	CDM	17.21 ± 0.26	2.35	1.21	0.20	3.77 ± 0.14	4565	185	330
446–13	N	108/184	16 ± 1	0.80(170)	CDM	16.92 ± 0.31	2.05	1.20	0.20	3.45 ± 0.13	4905	215	360
		97	10 ± 1	−0.34(68)	CDM	16.16 ± 0.20					4685	195	340
446–14	E	94/169	30 ± 3	1.09(215)	MDM	15.80 ± 1.04	2.35	1.34	0.20	3.89 ± 0.15	4065	310	395
(1)	(2)	(3)	(4)	(5)	(6)	(7)	(8)	(9)	(10)	(11)	(12)	(13)	(14)

Notes. The OSL age test year is CE 2020 and values are rounded to nearest 5 a. Uncertainties are given at the 68% level of confidence (1σ); those associated with the OSL age represent the overall error (σ$_{OE}$) that includes type A (σ$_A$) and B (σ$_B$) errors combined in quadrature. In Col. 3 (n), the number of grains producing accepted D$_e$ values is followed after the solidus by the number of grains meeting the minimum intensity criterion (Supplementary Information, Table SM2); the nominal total number of grains analysed was 500 for all samples except 446-13 (700).

(*Pinus* tp. *pinea/pinaster;* CNA4815). The remaining sample of oak (Fig. 3 a&b; *Quercus* sp. deciduous; Beta 657288) was selected in the absence of other short-lived specimens from this context. All the samples were from the lower deposits (Figs. 2 and 3) within contexts judged to be undisturbed.

4. OSL measurements and results

A standard preparation process for extracting and preparing quartz inclusions was followed (Aitken, 1985), producing coarse grains (150–250 μm dia.) suitable for single grain (SG) measurements; a SAR procedure (Murray and Wintle, 2003) was applied for the determination of the equivalent dose, D$_e$. All the OSL data used in calculations were derived from the analysis of a dominant fast OSL decay component. The presence of the latter was tested by employing a semi-quantitative procedure to inspect the form of decay, as discussed in the Supplementary Material (Sec. 1.4). Table 1 includes a summary of key data relevant to the calculation of the weighted mean value of $\overline{D}_e$ (col. 7) ordered by sample reference number (col. 1). The statistical dose model applied to calculate $\overline{D}_e$ (Galbraith and Roberts, 2012) is given in col. 6 (CDM, central dose model, or MDM, minimum dose model) using the number of accepted D$_e$ values given in col. 3. The latter formed a relatively high proportion (10–20%) of the number of grains analysed from each sample. Further details of the sample preparation, OSL measurement procedures and data analysis are given in the Supplementary Material.

The dose evaluation model was selected following an assessment of the distributions of accepted values of D$_e$ using quantile-quantile (Q-Q) plots (Fig. 4), and taking into account the extent of overdispersion (OD; Table 1, col. 4) calculated using a CDM and the weighted skewness, c, expressed as a percentage of the critical value (Table 1, col. 5; $c_{crit} = 2\sigma_c$; Arnold and Roberts, 2009; Bailey and Arnold, 2006). Where individual D$_e$ value ranges that overlap with the broken line shown in the Q-Q plots conform to a normal distribution (e.g., 446 -5 and −7), and supports the use of a CDM. Application of the latter is also appropriate where there is a small number of outliers in the lower and/or upper ranges of the distribution (e.g., 446 -2 and, −11) that are indicative of overdispersion. The D$_e$ distributions obtained with samples 446 -6 and −13 also conform to a normal distribution over a substantial proportion of D$_e$ values, but with significant deviations in their upper range. The skewness is sensitive to such deviations. In the case of sample 446-6, a significant positive skewness is neutralised (c = −0.09; c/c_{crit} = 27%) by removal of the highest D$_e$ value, and for sample 446-13 removal of the highest eleven D$_e$ values similarly reduces (c = −0.34; c/c_{crit} = 68%; n = 97) the positive skewness of the full set of data (c = −0.8; c/c_{crit} = 170%; n = 108). As

indicated in Table 1 (cols. 3 & 7), the removal of outliers in the uppermost range of D$_e$ values has a marginal effect on the calculation of the weighted average equivalent dose, $\overline{D}_e$, in the case of samples 446 -2 and −6 (<1%; 1 outlier removed) and a small effect for sample 446-13 (−4.5%; 11 outliers removed). While the D$_e$ distributions obtained with samples 446-3 and −14 follow a normal distribution within the central region, the presence of a divergent group of D$_e$ values in the lower range indicates that the adoption of a minimum dose model (MDM) may be appropriate. Both samples exhibit values of OD (30%) and skewness (c/c_{crit} ~200%) that are significantly higher than for the other samples, although the skewness is reduced substantially (c/c_{crit} = 44%) by the removal of the highest D$_e$ value in the case of sample 446-3. While the extent of deviation of the lower range of D$_e$ values from the line of conformity is visually less clear-cut in the Q-Q plot for sample 446-3, closer inspection of the D$_e$ values indicates that values below the median form a coherent group. The proportions of grains at gamma were 0.60 and 0.57 for samples 446-3 and −14 respectively. Hence, on the basis of these assessments, $\overline{D}_e$ was calculated by applying the CDM with all samples except 446 -3 and −14, where the MDM was applied.

5. Burial dose rate

The average burial dose rate was estimated on the basis of: measured specific activities of the lithogenic radionuclides in sediment samples and a sample representative of the granite monument using high resolution gamma spectrometry (HRGS; Supplementary Material, Sec. 2.1); the use of dose conversion factors (Guérin et al., 2011) and our own calculations (Bailiff et al., 2014) to calculate infinite medium dose rates; the application of radiation transport code to model the variation in gamma dose rate in close proximity to the granite monolith; the calculation of the cosmic dose rate using formulae given in Prescott and Hutton (1988, 1994). Table 1 contains a summary of the dose rate data (cols. 8–11) used to calculate the OSL age for each sample, including the beta ($\dot{D}_\beta$), gamma ($\dot{D}_\gamma$) and cosmic ($\dot{D}_c$) components of the dose rate, and the total dose rate, $\dot{D}_{tot}$ is given with its associated type A error. The beta and gamma dose rates shown are adjusted for moisture content (Aitken, 1985), where an average burial value of 15 ± 5% was assumed for all sediment samples. The beta dose rate also includes an adjustment for beta attenuation due to finite grain size (Brennan, 2003; Bailiff, 2018) and includes a contribution of 0.035 mGy a^{-1} to account for trace quantities of radionuclides within the quartz grains, based on a cumulative average for grains previously analysed by the laboratory. The total uncertainty was estimated by combining in quadrature the random errors associated with gamma spectrometer measurements, a 2% systematic error to account for instrument reproducibility, a 3% systematic
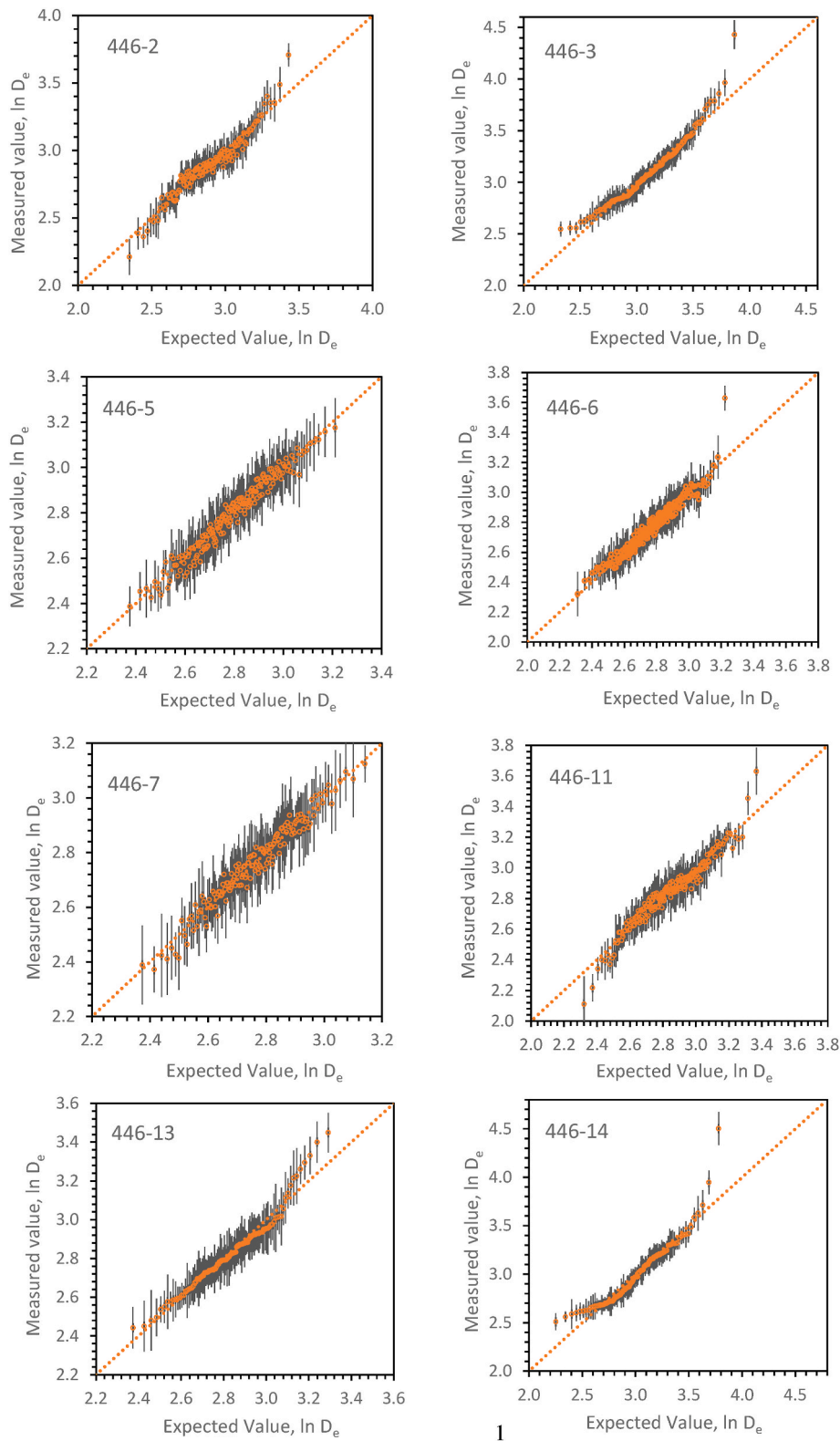
Fig. 4. Quantile-Quantile plots of expected vs measured D$_e$ data.

error on the dose rate conversion factors and a 2% systematic error associated with the beta attenuation correction factors.

The measured specific activities of lithogenic radionuclides are given in Table 2. At locations 3, 11 and 14, sampled using 25 mm dia. tubes, sediment portions were combined to provide a sufficient sample weight for the spectrometer measurements. Due to an instrument failure, it was

not possible to measure all the samples obtained, and in the case of locations 5, 6 and 13 the sediment activities were assumed to be similar to those for locations 7 and 8. For the group of sediment samples tested, the standard deviations of the specific activities of ^{232}Th, nat. U and ^{40}K were ±5%, ±8% and ±7% respectively. This spread mainly arises from difference in measured ^{40}K content between samples from the North and

Table 2

Specific activities and measure of disequilibria for lithogenic radionuclides in sediment and granite samples.

Sample	Type	Section	^{238}U (Bq kg^{-1})	^{232}Th (Bq kg^{-1})	^{40}K (Bq kg^{-1})	^{210}Pb/^{226}Ra
446–2	Sediment	E	68.3 ± 2.3	28.8 ± 3.3	820 ± 9	0.89 ± 0.05
446-3, 11, 14	"	E	68.1 ± 2.2	31.0 ± 3.2	909 ± 10	0.88 ± 0.05
446–4	"	E	78.3 ± 2.4	31.9 ± 3.4	940 ± 10	0.94 ± 0.05
446–7	"	N	61.6 ± 1.7	30.4 ± 2.5	775 ± 7	1.06 ± 0.05
446–8	"	N	65.5 ± 2.2	28.1 ± 3.2	757 ± 9	0.87 ± 0.05
446-G	Granite		44.2 ± 1.9	12.4 ± 2.9	540 ± 8	0.78 ± 0.07
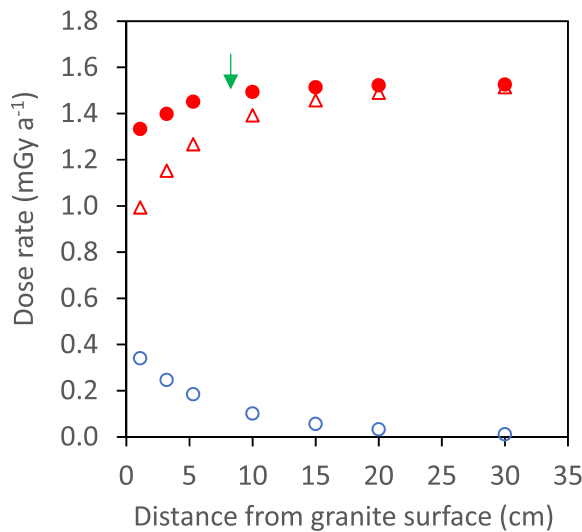
Fig. 5. Example of calculated dose-rate profiles for sample 446-2 calculated using the monolith model, as discussed in the main text and in the Supplementary Material. The profiles shown were calculated assuming uniformly distributed lithogenic sources in a) the granite slab (open circles) and b) in the surrounding sediment (open triangles); the sum of a) and b) is indicated by filled circles. The arrow indicates the relative position of the OSL sample tube.

East sections and these correspond to (maximal) differences in the beta and gamma infinite medium dose rates of 15% and 11% respectively. It is interesting to note that the granite is less radioactive than the sediment.

5.1. Modification of gamma dose rate by granite monolith

In the absence of on-site measurements, the gamma dose rate in the sediment medium within the proximity of the granite monolith was assessed using a simplified computational dosimetry model (Supplementary Material, Sec 2.2). Using the model simulations, the gamma dose rate in cylindrical volumes of sediment was calculated as a function of distance from the granite slab below ground level in a uniform sediment burial medium. Using the results of the simulations, the profile of average gamma dose rate within the detector volumes vs distance from the two orthogonal faces was calculated for the specified concentrations of each source type (^{40}K, Nat. U and ^{232}Th) located in each medium (Supplementary Material, Table SM3). The profiles were used to calculate the gamma dose rate at each sample location, an illustration if which is shown in Fig. 5 for sample 446-2, using the specific activity of the sediment measured for that sample. In this case, the modelled dose

Table 3

Radiocarbon samples and ages.

Laboratory Reference	Taxon	Strat. Unit	Context	Uncalibrated Age (BP)
CNA 4812	*Fraxinus* sp.	7	Containing prehistoric pottery	4020 ± 30
CNA 4815	*Pinus* tp. *pinea/ pinaster*	7	Socket pit underlying menhir base	6410 ± 35
Beta-657288	*Quercus* sp. *deciduous*	7	20 cm below base of menhir, containing prehistoric pottery	4130 ± 30
CNA 4813	*Fraxinus* sp.	8	Containing prehistoric pottery	4010 ± 30
Beta 525113	*Corylus avellana*	10	20 cm below base of menhir	4120 ± 30
CNA 4814	Fabaceae	10	"	4200 ± 30

Notes. CNA: Centro Nacional de Aceleradores, Seville, Spain; Beta: Beta Analytic, Miami, USA.

rate arising from the granite compensates for the reduction in the dose rate from the sediment in close proximity to the granite slab.

The total uncertainty in the gamma dose rate was estimated by combining in quadrature the random error associated with the HRGS activity measurements, a 2% systematic error to account for instrument reproducibility and a 5% systematic error associated with the model-derived dose rate.

5.2. Cosmic dose rate

The average cosmic dose rate was calculated assuming the overburden had been maintained throughout the burial period and using the site location (based on its coordinates, 41.74986° North; −7.67442° West) and elevation (884 m). In the absence of in situ dosimeter measurements to investigate the potential effect of the lithic monument on the effective depth of sediment samples, an average depth of 185 g cm^{-2} was assumed for all sample locations and a type A uncertainty of ±10% assigned to the dose rate. As recommended by Prescott and Hutton, a type B uncertainty of ±5% associated with the cosmic dose rate was included in the calculation of the overall uncertainty in the OSL age.

6. Age calculations

The OSL age (Table 1, col. 12), calculated as the quotient $\overline{D}_e/\dot{D}_{tot}$, is given with associated type A (col. 13) and overall (col. 14) errors, where the latter includes type A and B errors combined in quadrature. The uncertainties are given at the 68% level of confidence (1σ). The additional age calculation for sample 446-13 corresponds to the use of a reduced set of D_e values, as discussed above.

Calculation of pooled mean OSL ages (type A errors) for the socket pit deposit samples from the North (446–5, −6, −7 and −13) and East (446 -3, −11 and −14) sections, 4602 ± 96 a (T = 0.4; $\chi^2_{3,0.05} = 7.81$) and 4443 ± 144 a (T = 2.0; $\chi^2_{2,0.05} = 5.99$), respectively, indicate that each form a coherent group (Ward and Wilson, 1978). In the North section group, the age adopted for sample 446-13 (4685 ± 195 a) was calculated using the reduced set of D_e values, as discussed above. Comparison of the pooled mean age for the socket pit samples and sample 446-2 taken from adjacent deposits within Unit 7 of the East section indicate that the difference is not significant (T = 2.6; $\chi^2_{1,0.05} = 3.84$). Its inclusion moves the pooled mean age (4572 ± 120 a; T = 5; $\chi^2_{4,0.05} = 7.8$) for all the East section sample ages in closer agreement with that for the North section. Comparison of all the ages for North and East sections indicate that they also form a coherent group, with a pooled mean age of 4590 ± 283 a (T = 5.0; $\chi^2_{7,0.05} = 14.1$; type B errors).
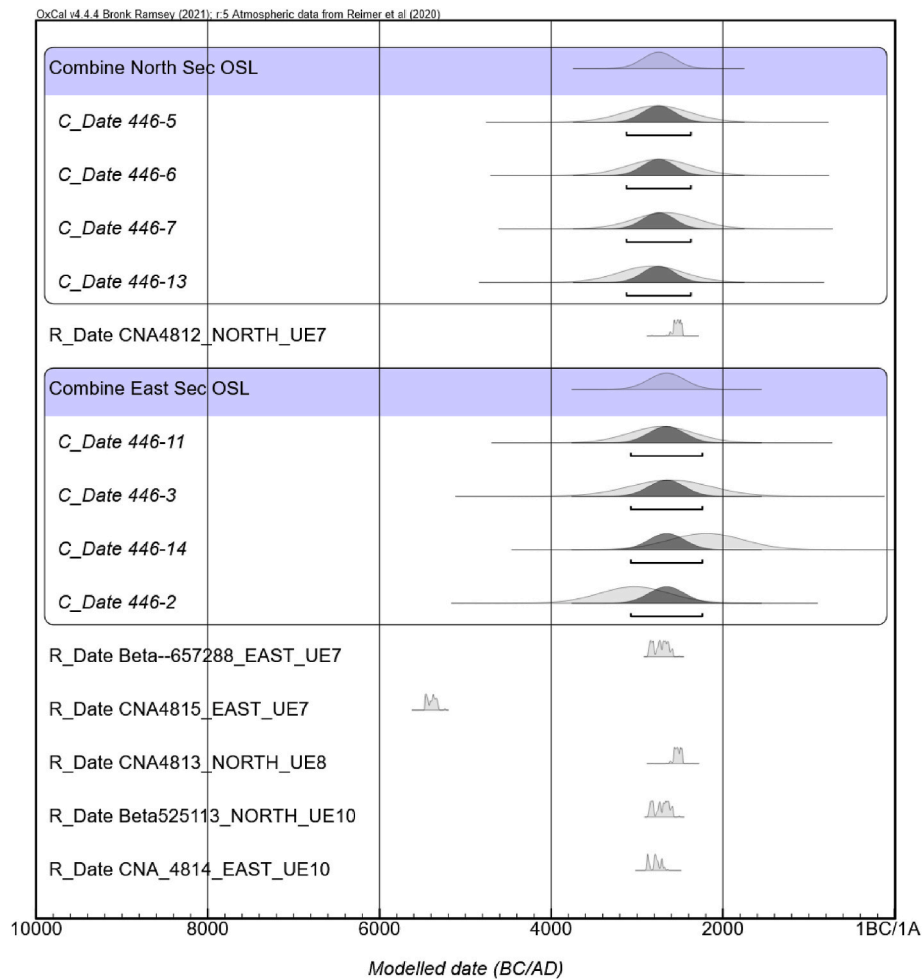
The uncalibrated radiocarbon ages are listed in Table 3,

Fig. 6. Bayesian model incorporating OSL and radiocarbon age results.

accompanied by the calibrated ranges obtained using OxCal Ver 4.4.4 (Bronk-Ramsey, 2021), which was also used to construct a simple chronostratigraphic Bayesian model (Fig. 6). While all but one of the samples are short-lived, in the case of the oak sample (Beta 657288) an old wood offset cannot be ruled out as it is not confirmed to originate from a young branch, and oak is a long-lived species. While there is uncertainty regarding its original location within the tree, the radiocarbon age is consistent with the ages obtained for the short-lived samples. As discussed above, the remaining samples were attributed to young growth, and consequently without an old wood offset. However, for all charred samples, there is the additional issue of the time elapsed between removal from the exchange reservoir and its combustion, either in a hearth or during a fire, whether anthropogenic or natural. As no hearth was identified within the limits of the excavation, the cause of combustion is unknown. The identified grouped charcoals may correspond to a mixture of charcoals of different origins. Although this cannot be clarified on the basis of archaeological data currently available, examination of the sample of *Pinus* charcoal indicates that it is likely to be the result of a vegetation fire of anthropic or natural origin.

The combined pooled mean OSL date range for North and East sections (2289–2855 BCE; 1σ) overlaps (Fig. 6) with the calibrated radiocarbon ages for the two samples (CNA 4812 and 4813) taken from the stratigraphically most closely related deposits in Units 7 and 8, which, when combined, have a pooled mean age range of 2571–2476 BCE (1σ). Although appearing visually to be slightly earlier than the latter, a difference between the radiocarbon ages for UE7/8 and UE10 is not fully resolved as the model estimates date ranges for the end of the deposition of UE10 (2818-2464 BCE; 1σ) and for the start of UE7/8 (2663-2488

BCE; 1σ). The radiocarbon age (5470-5327 BCE; 1σ) for sample CNA 4815 (*Pinus*), which was located directly below the base of the monument, appears to be an outlier when compared with the other radiocarbon and OSL ages, being substantially older than the other charcoal samples. This result suggests that the sample is likely to be associated with the removal of charcoal that was related to earlier fire events in the area during the construction process. The radiocarbon age is consistent with the degradation of forest cover in the Northwest area of Iberia involving the use of fire during the period ca 6000-4000 BCE that had been identified by Kaal et al. (2011).

7. Discussion

The OSL results obtained indicate that for the majority of samples the exposure of grains to daylight during setting of the monument was sufficient to optically reset the fast OSL decay component. The two samples (446-3 and −14) where the form of the D_e distributions were interpreted to reflect partial optical bleaching before burial were closely located within the socket fill deposits near its base in the East section. Although, as discussed above, the OSL dates for these and the other socket fill deposits form a coherent group, the slightly younger depositional age for sample 446–14 may flag the potential for the MDM to underestimate the burial dose. Given the potential for disturbance and the mixing of deposits, sampling a series of locations from the context(s) of primary interest – in this case the base of the monolith - enables the consistency of the age estimates to be tested. Also, the extension of the full D_e distributions to significantly higher values for these two samples compared with those for samples 446 -2 and −5 located in UE7, for

example, is indicative of the presence of grains drawn from sediment of significantly greater depositional age. This may also account for the presence of the sample of *Pinus* recovered from the base of the socket lying below samples 446-3 and −14 in the socket fill deposits that produced a significantly earlier radiocarbon date.

8. Conclusion

The concordance of the OSL and radiocarbon chronologies is very encouraging and provides the basis for more detailed work on monuments of this type. The mid-3rd millennium radiocarbon and OSL dates confirm the original setting during the Copper Age and consequently, on the basis of the iconography, a later (possibly Early Bronze Age) 'recycling' of the monolith including carving of the sword should be considered. Where permitted excavation allows access to the socket pit of a standing stone, OSL has the potential to provide reliable dating of depositional processes related to the construction process, and, together with other recent work (e.g., Gliganic et al., 2023), contributes to widening its scope for dating standing and recumbent stone monuments. In more detailed work, the application of OSL coupled with micromorphological analysis would provide a valuable tool for the reconstruction of site formation processes associated with setting of the statue-menhir and any subsequent modification of the site, which generally is a potential issue of central importance in the case of standing stone monuments. Aspects such as micromorphological analysis of sediment structure, the in situ measurement of dose rate and a more detailed examination of the depositional history associated with the setting of the statue-menhir await further fieldwork. An account of the archaeological fieldwork and its interpretation including the application of the dating results will be published elsewhere (Diaz-Guardamino et al., in preparation).

Appendix A. Supplementary data

Supplementary data to this article can be found online at https://doi.org/10.1016/j.quageo.2024.101569.

References

Aitken, M.J., 1985. Thermoluminescence Dating. Academic Press, London.

Alves, L.B., Reis, M., 2011. Memoriais de pedra, símbolos de identidade. As estelas decoradas de Cervos (Montalegre). In: Vilaça, R. (Ed.), Estelas e Estátuas-menir: da Pré à Proto-história. Câmara Municipal do Sabugal, Sabugal +, Centro de Estudos Arqueológicos das Universidades de Coimbra e Porto (CEAUCP) e Instituto de Arqueologia do DHAA da FLUC, pp. 187–216.

Arnold, L.J., Roberts, R.G., 2009. Stochastic modelling of multi-grain equivalent dose (De) distributions: implications for OSL dating of sediment mixtures. Quat. Geochronol. 4, 204–230.

Bailiff, I.K., 2018. An examination of beta dose attenuation effects in coarse grains located in sliced samples. Radiat. Meas. 120, 188–194.

Bailiff, I.K., French, C.A., Scarre, C.J., 2014. Application of luminescence dating and geomorphological analysis to the study of landscape evolution, settlement and climate change on the Channel Island of Herm. J. Archaeol. Sci. 41, 890–903.

Bailey, R.M., Arnold, L.J., 2006. Statistical modelling of single grain quartz De distributions and an assessment of procedures for estimating burial dose. Quat. Sci. Rev. 25, 2475–2502.

Brandherm, D., 2003. Die Dolche und Stabdolche der Steinkupfer- und älteren Bronzezeit auf der Iberischen Halbinsel, vol 12. Franz Steiner Verlag, Suttgart, Germany.

Brennan, B.J., 2003. Beta doses to spherical grains. Radiat. Meas. 37, 299–303.

Bronk Ramsey, C., 2021. OxCal 4.4.4. Available from: http://c14.arch.ox.ac.uk/oxcal. (Accessed 25 October 2023).

Bueno Ramirez, P., Balbín Behrmann, R., Barroso Bermejo, R., 2016. Megalithic art in the iberian peninsula. Thinking about graphic discourses in the European megaliths. Préhist. Méditerranéennes 185–203. https://doi.org/10.4000/books.pup.4809.

Bueno Ramírez, P., Barroso Bermejo, R., De Balbín Behrmann, R., Salvado, P., 2019. Stone witnesses: armed stelae between the international tagus and the douro, iberian peninsula. SPAL - Revista de Prehistoria y Arqueología 28, 143–164. https://doi.org/10.12795/spal.2019.i28.17.

Calado, M., 2002. Standing stones and natural outcrops. The role of ritual monuments in the Neolithic transition of the Central Alentejo. In: Scarre, C. (Ed.), Monuments and Landscapes in Atlantic Europe. Perception and Society during the Neolithic and the Bronze Age. Routledge, UK, pp. 17–35.

Cartwright, C.R., 2015. The principles, procedures and pitfalls in identifying archaeological and historical wood samples. Ann. Bot. 116, 1–13.

Cassen, S. (Ed.), 2009. Autour de la Table. Explorations archéologiques et discours savants sur des architectures néolithiques à Locmariaquer, Morbihan (Table des Marchands et Grand Menhir). Laboratoire de recherches archéologiques, CNRS and Université de Nantes. Nantes.

Comendador Rey, B., 1995. Caracterización de la metalurgia inicial gallega: una revisión. Trab. Prehist. 52, 111–130.

Díaz-Guardamino, M., 2010. Las estelas decoradas en la Prehistoria de la Península Ibérica. Universidad Complutense de Madrid, Madrid. PhD thesis.

Díaz-Guardamino, M., Alves, L.A., et al., n.d. in preparation. The temporality of statue-menhirs in Iberia: the statue-menhir at Cruz de Cepos. Cervos, Montalegre, North Portugal.

Galbraith, R.F., Roberts, R.G., 2012. Statistical aspects of equivalent dose and error calculation and display in OSL dating: an overview and some recommendations. Quat. Geochronol. 11, 1–27.

Gliganic, L.A., Slack, M., Meyer, M.C., 2023. Tending to tradition: dating stone arrangement maintenance in northwest Australia using optical methods. J. Archaeol. Sci.: Report 49, 104053.

Gomes, M.V., 1993. O Marco de Anta ou estela-menir de Caparrosa (Tondela, Viseu). Estudos Pré-Históricos 1, 7–27.

Gómez Ramos, P., 2001. La espada de La Perla. Estudio de las empuñaduras de remaches con doble arco: un *Unicum* en la serie de armas europeas de la Edad del Bronce. Gladius 21, 5–29. https://doi.org/10.3989/gladius.2001.78.

Guérin, G., Mercier, N., Adamiec, G., 2011. Dose-rate conversion factors: update. Ancient TL 29, 5–8.

Jorge, S.O. (Ed.), 1995. A Idade do Bronze em Portugal. Discursos de poder. Museu Nacional de Arqueología, Lisbon.

Kaal, J., Carrión Marco, Y., Asouti, E., Martín-Seijo, M., Martínez-Cortizas, A., Costa Casáis, M., Criado Boado, F., 2011. Long-term deforestation in NW Spain: linking the Holocene fire history to vegetation change and human activities. Quat. Sci. Rev. 30, 161–175.

Large, J.-M., Mens, E., 2016. The stone rows of Hoedic (Morbihan) and the construction of alignments in western France. In: Laporte, L., Scarre, C. (Eds.), The Megalithic Architectures of Europe. Oxbow, Oxford, pp. 183–195.

Marguerie, D., Hunot, J.Y., 2007. Charcoal analysis and dendrology: data from archaeological sites in north-western France. J. Archaeol. Sci. 34, 1417–1433.

Murray, A.S., Wintle, A.G., 2003. The single aliquot regenerative dose protocol: potential for improvements in reliability. Radiat. Meas. 37, 377–381.

Prescott, J.R., Hutton, J.T., 1988. Cosmic ray and gamma ray dosimetry for TL and ESR. Radiat. Meas. 14, 223–227.

Prescott, J.R., Hutton, J.T., 1994. Cosmic ray contribution to dose rates for luminescence and ESR dating: large depths and long-term time variations. Radiat. Meas. 23, 497–500.

Ward, G.K., Wilson, S.R., 1978. Procedures for comparing and combining radiocarbon age determinations: a critique. Archaeometry 20, 19–31.

Whittle, A., 2002. Conclusion: long conversations, concerning time, descent and place in the world. In: Scarre, C. (Ed.), Monuments and Landscape in Atlantic Europe. Perception and Society during the Neolithic and Early Bronze Age. Routledge, UK, pp. 192–204.